Electron tunneling in protein crystals

F. Akif Tezcan, Brian R. Crane[†‡], Jay R. Winkler[‡], and Harry B. Gray[‡]

Beckman Institute, MC 139-74, California Institute of Technology, Pasadena, CA 91125

Contributed by Harry B. Gray, February 13, 2001

The current understanding of electron tunneling *through* proteins has come from work on systems where donors and acceptors are held at fixed distances and orientations. The factors that control electron flow *between* proteins are less well understood, owing to uncertainties in the relative orientations and structures of the reactants during the very short time that tunneling occurs. As we report here, the way around such structural ambiguity is to examine oxidation–reduction reactions in protein crystals. Accordingly, we have measured and analyzed the kinetics of electron transfer between native and Zn-substituted tuna cytochrome *c* (cyt *c*) molecules in crystals of known structure. Electron transfer rates [(320 s^{-1} for *Zn-cyt *c* → Fe(III)-cyt *c*; 2000 s^{-1} for Fe(II)-cyt *c* → Zn-cyt c^+)] over a Zn–Fe distance of 24.1 Å closely match those for intraprotein electron tunneling over similar donor–acceptor separations. Our results indicate that van der Waals interactions and water-mediated hydrogen bonds are effective coupling elements for tunneling across a protein–protein interface.

Extensive experimental and theoretical investigations have elucidated the role of polypeptide structure in facilitating electron tunneling through proteins (1–13). Most of the definitive work has centered on molecules with fixed donor–acceptor distances and orientations, such as proteins covalently modified with redox-active units (1–5) or proteins that contain both donors and acceptors (6, 7). This work has established that the dependence of rate on distance is exponential (1, 2, 12, 13), as expected for a tunneling reaction (8), with decay constants in the 1.0- to 1.2-$Å^{-1}$ range (1, 2, 13). It is likely, therefore, that the redox centers in these proteins are coupled electronically through the chemical-bond framework of the intervening medium (1–6, 8, 11).

Electron transfer (ET) between proteins is understood less well, as it involves at least three steps: (*i*) association of the donor and acceptor; (*ii*) electron tunneling within the donor–acceptor complex; and (*iii*) dissociation of the oxidized and reduced products (14–16). Because the dynamics of the first and the third steps obscure the electron tunneling reaction, many studies have focused on the ET properties of stable protein–protein complexes in solution (5, 15, 17). It has been difficult to interpret the results, however, as neither the donor–acceptor docking geometries nor the conformations of these complexes are known. Studies of kinetics and structure under the same conditions are needed to probe the interactions that promote electron tunneling between proteins.

A protein crystal containing photoactivatable donors and acceptors at specific lattice sites is an ideal medium for investigating the dependence of tunneling rates on structure.[§¶] In the crystal lattice of tuna cytochrome *c* (cyt *c*) (23), chains of cyt *c* molecules form helices with a 24.1-Å separation between neighboring metal centers (Fig. 1). All other metal–metal distances in the lattice are greater than 30 Å, with estimated electron tunneling times that are at least three orders of magnitude slower (2). Thus, the heme groups can be treated as ordered in a one-dimensional chain, separated by identical protein and solvent media. By doping Zn-cyt *c* into this lattice (Table 1), interprotein ET reactions can be triggered by laser excitation (Scheme 1). The triplet state of Zn-cyt *c* (*Zn-cyt *c*) is generated in high yield with 550- or 580-nm excitation (**R1**). This highly reducing excited state ($E^0 \approx -0.8$ V) reacts with Fe(III)-cyt *c* ($E^0 \approx 0.25$ V) to generate Fe(II)-cyt *c* and the Zn-cyt *c* cation radical, Zn-cyt c^+ ($E^0 \approx 0.9$ V) (**R2**) (24). In a dark reaction, Zn-cyt c^+ and Fe(II)-cyt *c* recombine to yield the ground-state species (**R3**). Of special interest is our finding that the rates of tunneling reactions across a protein–protein interface (**R2**, **R3**) closely match those for intraprotein ET over similar donor–acceptor separations.

Materials and Methods

Crystallization Conditions. Tuna heart cyt *c* (Sigma) was used as received. Zn- and Co-cyt *c* were prepared according to established procedures (24, 25). Zn:Fe-cyt *c* cocrystals were grown at room temperature in sitting or hanging drops. The reservoir solution contained 500 μl of 70–85% saturated $(NH_4)_2SO_4$, 0.75 M NaCl, and 0.1 M NaP_i (pH 6.0), and the drops were 2 μl of 4–10 mM protein and 2 μl of reservoir solution. Crystal growth is governed by the Fe(III) protein, which nucleates rapidly (few hours) to produce large rod-shaped crystals ($500 \times 50 \times 50$ μm), rather than the Zn protein, which crystallizes slowly (>2 weeks) in higher $(NH_4)_2SO_4$ concentrations (≈85% saturated) to give bundles of thin needles ($500 \times 5 \times 5$ μm).

Structure Determination. The structures of Fe:Zn-cyt *c* cocrystals were determined by refinement of a model from isomorphous crystals of tuna heart cyt *c* (Protein Data Bank ID code 3CYT) (23) against diffraction data processed with DENZO (26). Rigid-body, simulated-annealing, positional, and thermal refinement with CNS (27), amidst rounds of manual rebuilding, and water placement with XFIT (28) produced the final models (Table 1). Superimposed, noninteracting Fe and Zn porphyrins were refined simultaneously for each cyt *c* molecule. Stereochemical restraints were removed from the heme axial ligand bonds in the later stages of refinement. Solvent-accessible surface area was calculated by using MS (29). Interatomic separations between 3.2 and 3.9 Å defined van der Waals contacts. Water molecules within 3.9 Å of both proteins were assigned as interfacial. Fe:Zn occupancies were defined by using multiwavelength anomalous diffraction data collected at the Stanford Synchrotron Radiation Laboratory BL-92 on crystals grown out of 2Fe:1Zn and 1Fe:2Zn solution stoichiometries. For each crystal, metal occu-

---

Abbreviations: ET, electron transfer; cyt *c*, cytochrome *c*; *Zn-cyt *c*, triplet excited state of Zn-substituted cyt *c*; CcP, cyt *c* peroxidase.

Data deposition: The atomic coordinates have been deposited in the Protein Data Bank, www.rcsb.org [PDB ID codes 1I54 (2Fe:1Zn-cyt *c*) and 1I55 (1Fe:2Zn-cyt *c*)].

[†]Present address: Department of Chemistry and Chemical Biology, Cornell University, Ithaca, NY 14853.

[‡]To whom reprint requests should be addressed. E-mail: crane@bonobo.chem.cornell.edu, winklerj@caltech.edu, or hbgray@caltech.edu.

[§]Feher and colleagues (18) have measured the kinetics of photoinduced ET between the photosynthetic reaction center and cyt c_2 (*Rhodobacter sphaeroides*) complexed in crystals. However, the low resolution (3.5 Å) of this structure and poor cyt c_2 electron density did not allow a precise definition of the polypeptide and solvent medium between the electron donor (cyt c_2 heme) and the acceptor (bacteriochlorophyll dimer).

[¶]Crystal structures of four redox protein complexes have been determined: cyt *c*-cyt *c* peroxidase (CcP; ref. 19); methylamine dehydrogenase-amicyanin (20); methylamine dehydrogenase-amicyanin-cyt c_{551i} (21); and FMN-cytochrome P450BM-3 (22). The kinetics of electron tunneling reactions in these crystals have not been measured.

The publication costs of this article were defrayed in part by page charge payment. This article must therefore be hereby marked "*advertisement*" in accordance with 18 U.S.C. §1734 solely to indicate this fact.

www.pnas.org/cgi/doi/10.1073/pnas.081072898

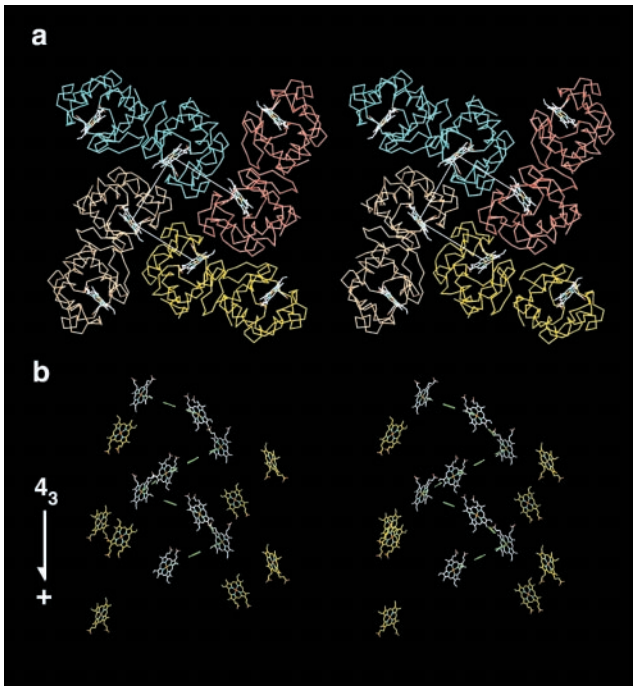

Fig. 1. Stereoviews of cyt *c* crystal packing (space group $P4_3$). The asymmetric unit contains two molecules, with one related to a 4_3 axis at the unit cell origin and the other related to a second 4_3 axis at the unit cell center. The two screw axes run antiparallel to each other and are related by a pseudotwofold axis directed along the *ab* diagonal. This packing produces a 24.1-Å separation between the metal centers of adjacent molecules (Mol_i and Mol_{i+1}) within each screw axis. (*a*) View down the $P4_3$ axis. Different colors indicate pairs of cyt *c* molecules in the same asymmetric unit. White lines connect the iron centers that are separated by 24.1 Å. (*b*) View of heme orientation along the $P4_3$ axis. Broken lines connect the hemes that are involved in ET reactions.

pancy refinement with MADPHSREF (30) was carried out against data sets collected at four energies [7124, 7135, 9666, and 9671 eV (1 eV = 1.602×10^{-19} J)] chosen to accentuate both the absorptive and dispersive components of Fe and Zn anomalous scattering.

Kinetics Measurements. Crystals for transient absorption experiments were mounted and sealed inside 1 × 1 mm quartz capillaries in an anaerobic tent to prevent oxidative photodegradation of Zn-cyt *c*. If crystals were grown outside the tent, they were soaked in deaerated solutions for at least 2 days before kinetics measurements. Once deaerated, the crystals were resistant to photodegradation indefinitely. Transient absorption spectroscopy was carried out with a 75-W Xe-arc lamp probe light source, a microspectrophotometer to focus (≈100 μm diameter at the sample) and to collect the probe light, and a Nd:YAG pumped optical parametric oscillator (OPO) as the pump light source. Output from the OPO (550 or 580 nm) was used for excitation of Zn-cyt *c*. Large crystals [≈50 μm (width) × 50 μm (depth)] consistently exhibited reproducible kinetics; when only smaller crystals were available, they were clustered together to prevent excess stray probe light. Generally, no visible damage to crystals by laser excitation was observed even at high pulse energies (≥4 mJ). Owing to the intense absorption of *Zn-cyt *c* or Zn-cyt c^+, extensive signal averaging was not necessary (≤25 shots at 470 or 675 nm). Kinetics were fit by a nonlinear least-squares routine.

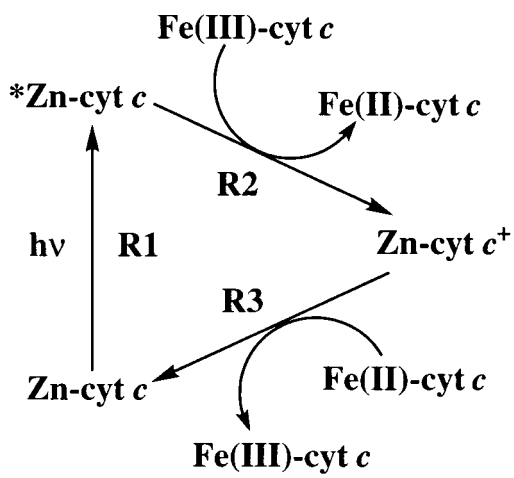

Scheme 1. Zn-cyt *c* redox photochemistry.

Table 1. X-ray data collection, refinement, and metal occupancy statistics for tuna Fe:Zn-cyt *c* structures

Stoichiometry*	2Fe:1Zn	1Fe:2Zn
Residues	103 + 1 heme	103 + 1 heme
Water molecules	488	488
Symmetry group	$P4_3$	$P4_3$
Unit cell dimensions, Å	74.18 × 74.18 × 35.54	74.36 × 74.36 × 35.70
Resolution, Å	30.0–1.5	30.0–2.0
X-ray wavelength, Å	1.54	1.28
Completeness, %	89.0	81.7
$\langle I/\sigma I\rangle$†	19.3	17.1
R_{sym}, %‡	6.6	6.2
R, %§	22.9	22.0
Free *R*, %¶	25.1	24.4
rmsd bond, Å‖	0.008	0.008
rmsd angle, °‖	1.4	1.4
Fe:Zn occupancy**	0.68:0.32	0.39:0.61
Average temperature factor, Å²		
Main-chain atoms	12.58	18.08
Side-chain atoms	12.74	18.12
Water molecules	23.46	29.98
Metal–ligand bond distances, Å		
His-18	(2.00)†† 2.00	2.00
Met-80	(2.27)†† 2.44	2.50‡‡

*Approximate stoichiometry of the crystallization solution.
†Intensity signal-to-noise ratio.
‡$R_{sym} = \Sigma\Sigma_j|I_j - \langle I\rangle|/\Sigma\Sigma_j|I_j|$.
§$R = \Sigma||F_{obs}| - |F_{calc}||/\Sigma|F_{obs}|$ for all reflections (no σ cutoff).
¶Free *R* calculated against 8% of the reflections removed at random.
‖Root-mean-square deviations (rmsd) from ideal bond and angle restraints.
**Relative occupancies of Fe and Zn as determined by multiwavelength anomalous diffraction experiments. For 2Fe:1Zn, different crystals were used for structure and metal-occupancy determinations. Values are averages of the two molecules in the asymmetric unit.
††Fe(III)-only cyt *c* (Protein Data Bank ID code 3CYT).
‡‡The increase in the Met-80 bond length with increasing Zn occupancy indicates that for Zn-only cyt *c*, $d_{Met\text{-}80} \geq 2.50$ Å.

Results and Discussion

We initially looked for ET by measuring the decay kinetics of *Zn-cyt *c* using transient absorption spectroscopy. *Zn-cyt *c* has intense absorption in the 450- to 500-nm range, whereas the ground-state molecule does not. In pure Zn-cyt *c* crystals, the excited-state decay could be fit satisfactorily to a monoexponential function with a rate constant of $\approx 80\ s^{-1} = k_{int}$, intrinsic decay rate constant), similar to that measured in solution (Fig. 2*a*) (24).

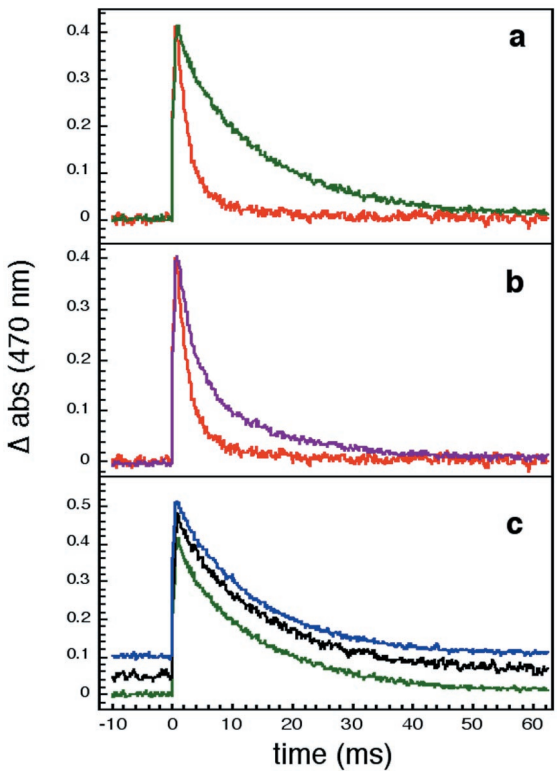

Fig. 2. *Zn-cyt *c* decay kinetics monitored at 470 nm. Δ absorbances are normalized. (*a*) Pure Zn-cyt *c* (green) and 2Fe(III):1Zn-cyt *c* (red). (*b*) 2Fe(III):1Zn-cyt *c* (red) and 1Fe(III):1Zn-cyt *c* (purple). (*c*) Pure Zn-cyt *c* (green); Fe(II): Zn-cyt *c* (black); and Co(III): Zn-cyt *c* (blue). The second and third traces are offset for clarity.

In Fe(III):Zn-cyt *c* cocrystals, the decay is considerably faster and better described by a biexponential function (Fig. 2 *a* and *b*). We assign the fast phase (k_{fast} = 400 ± 100 s^{-1}) to ET from *Zn-cyt *c* to Fe(III)-cyt *c* (**R2**), where the electron tunneling rate ($k_{ET} = k_{fast} - k_{int}$) is 320 s^{-1}.‖ The slower phase (k_{slow} = 70 ± 20 s^{-1}) closely matches the intrinsic decay of *Zn-cyt *c*, which is consistent with a distribution of cyt *c* molecules in the crystals; a fraction of Zn-cyt *c* molecules is adjacent to only two other Zn molecules and hence decay without undergoing an ET process. Accordingly, the amplitude of the slow phase grows relative to the fast phase as the Zn fraction in the cocrystals increases (Fig. 2*b*).

As controls, we examined Fe(II):Zn-cyt *c* and Co(III):Zn-cyt *c* cocrystals—ET in the former case is disfavored thermodynamically, whereas in the latter case there is a large barrier, owing to a high Co(III/II) reorganization energy (>2.4 eV) (25). *Zn-cyt *c* decay in both cases was slow and monoexponential, with rate constants [68 s^{-1} for Fe(II) and 78 s^{-1} for Co(III)] that were essentially the same as those observed in pure Zn-cyt *c* crystals (Fig. 2*c*). Zemel and Hoffman (31) reported fast *Zn-porphyrin (*Zn-P) decay at high pulse energies attributable to triplet–triplet energy transfer in Zn hemoglobin (24.1-Å metal–metal separation). Although a similarly fast decay channel was apparent in pure Zn-cyt *c* crystals (>4 mJ per pulse), it was less than 20% of the total amplitude at the pulse energies (<800 μJ) used in our experiments. Moreover, no such power dependence of the excited-state decay was observed in Fe(III):Zn-cyt *c* cocrystals, indicating that the contribution of triplet–triplet energy transfer to the fast decay kinetics was negligible.

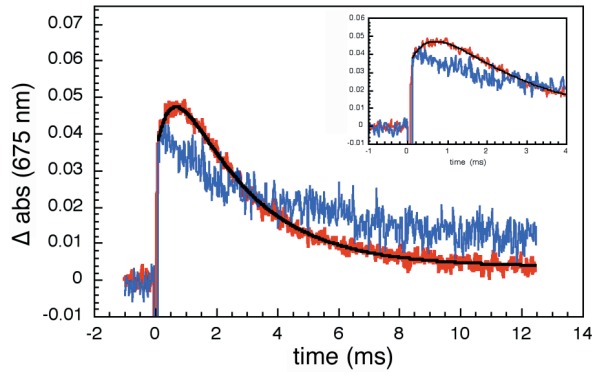

Fig. 3. Transient absorption (675 nm) kinetics. The prompt absorbance increase in pure Zn-cyt *c* crystals (blue) is caused by the generation of *Zn-cyt *c*. In 2Fe:1Zn-cyt *c* cocrystals (red), there is an additional rise attributable to the Zn-porphyrin cation radical, Zn-cyt c^+. The negative signal following the laser flash results from Zn-cyt *c* fluorescence. (*Inset*) A view of early kinetics from 2Fe:1Zn-cyt *c* cocrystals showing the rounded feature.

The search for ET products proved to be challenging. First, absorbance measurements in the Soret region are precluded in crystals, owing to high extinction coefficients ($abs_{424} \approx 65$ for a 50-μm thick crystal), and second, Fe(II)-cyt *c* formation in the Q-band region is difficult to monitor, as the isosbestic point for Zn-cyt *c* and *Zn-cyt *c* (540 nm) coincides with that for Fe(II)- and Fe(III)-cyt *c*. Our efforts to detect Zn-cyt c^+ were successful, because in the deep red region of the spectrum the molar absorbance of this cation radical greatly exceeds that of *Zn-cyt *c* (24). The transient kinetics probed at 675 nm reveal a prompt absorbance increase caused by *Zn-cyt *c* formation, followed by a slower rise corresponding to production of Zn-cyt c^+ (Fig. 3). The time constant for the subsequent decay of the 675-nm absorbance matches that measured at 470 nm (Fig. 2), indicating that charge recombination (**R3**) is faster than charge separation (**R2**). A biexponential fit to the 675-nm data yields the following rate constants: 400 ± 100 s^{-1} (k_{ET} = 320 s^{-1}) for **R2** and 2,000 ± 500 s^{-1} for **R3**.

Rapid relay of electrons by redox enzymes necessarily involves short-lived, weakly bound protein–protein complexes. The recognition sites between proteins in such complexes tend to be smaller (<1,200 $Å^2$) and include more water molecules than the interfaces between subunits in oligomeric proteins (32). In fact, the protein–protein interface between cyt *c* and CcP (770 $Å^2$) (19) is very small compared with other interfaces; there are 17 van der Waals contacts and 13 water molecules (two of which form bridging hydrogen bonds across the interface) but only one direct hydrogen bond bridging the two proteins. The interprotein interactions in crystals of tuna cyt *c* are similar (Fig. 4): 760 $Å^2$ of surface area is buried in an interface with 31 van der Waals contacts, 16 water molecules (3 bridging), and one direct hydrogen bond.** In addition, a heme vinyl group makes direct contacts across the interface in both the cyt *c*–cyt *c* and the

‖The rate constant for the fast phase increases (from 350 s^{-1} for 1Fe:2Zn up to 510 s^{-1} with 2Fe:1Zn cocrystals) as the relative Fe-cyt *c* concentration is raised. This observation is consistent with an increase in the fraction of Zn-cyt *c* molecules adjacent to two Fe-cyt *c* molecules (instead of one), whose excited-state decay rate ($k_{fast,\ 2}$) should be faster by k_{ET} ($k_{fast,\ 2} \approx 2\ k_{ET} + k_{int}$). Although the observed decay kinetics should be described by a triexponential function, it has not been possible to extract statistically significant values of k_{fast} and $k_{fast,\ 2}$ from fits to the single-crystal ET kinetics. Instead, increasing contributions from $k_{fast,\ 2}$ lead to larger values for the k_{fast} component in the biexponential fits.

**Direct comparison of cyt *c*–cyt *c* and cyt *c*–CcP interfaces is limited by differences in the respective resolution of the structures (1.5 Å vs. 2.3 Å) and disorder in the cyt *c*–CcP complex that leads to high thermal factors for cyt *c* (⟨*B*⟩ = 51.7 $Å^2$), interfacial water molecules (⟨*B*⟩ = 50.6 $Å^2$), and interfacial CcP residues (⟨*B*⟩ = 35.3 $Å^2$). The interfacial water molecules (⟨*B*⟩ = 19.2 $Å^2$) and residues (⟨*B*⟩ = 10.6 $Å^2$) in the cyt *c*–cyt *c* complex are well ordered.

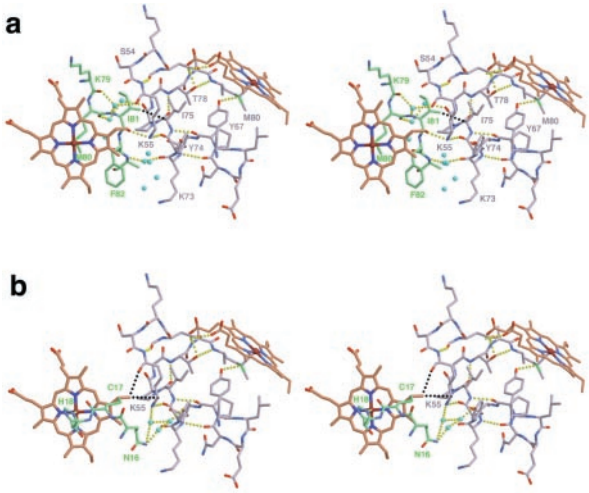

Fig. 4. Stereoview of heme groups (brown) and the intervening protein and solvent medium. Residues below (*a*) and above (*b*) the heme plane on the left-hand side are shown separately. The side- and main-chain atoms of 14 residues on each molecule participate in the interface, burying 400 Å^2 of solvent-accessible surface area on Mol$_i$ (green) and 360 Å^2 on Mol$_{i+1}$ (gray). Close contacts (black traces) in the interface include those between Ile-81$_i$ and Ile-75$_{i+1}$, and the heme vinyl$_i$ and Lys-55$_{i+1}$. The side chain of Lys-55$_{i+1}$ and the peptide carbonyl of Ile-81$_i$ form the only direct protein–protein hydrogen bond (yellow traces). Water-bridged hydrogen bonds link the main chain of Phe-82$_i$ to that of Lys-73$_{i+1}$, the side chain of Asp-16$_i$ to that of Lys-55$_{i+1}$, and the main chain of Ile-81$_i$ to both the main and side chains of Lys-55$_{i+1}$. A series of two or more water molecules (blue spheres) mediate additional hydrogen bonds between interfacial residues.

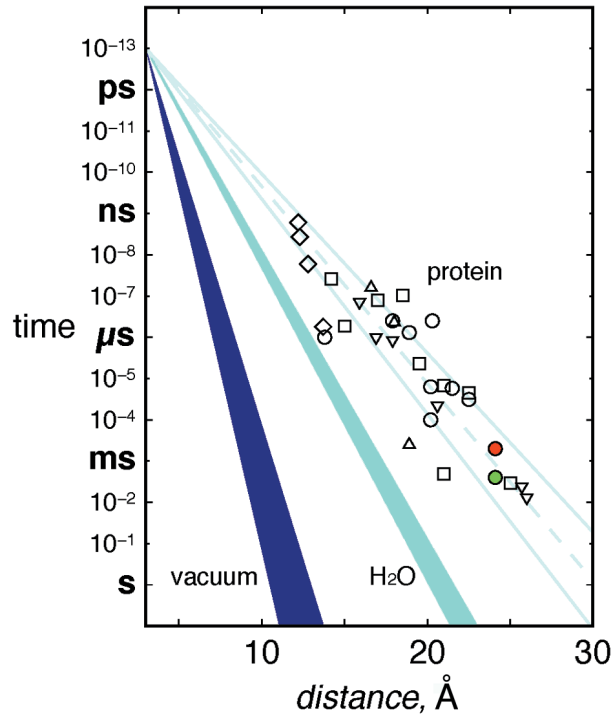

Fig. 5. Tunneling timetable for ET in Ru-modified proteins (open symbols), water (light blue, $\beta = 1.61–1.75$ Å^{-1}), and vacuum (dark blue, $\beta = 3.0–4.0$ Å^{-1}) (adapted from ref. 36). Most coupling-limited electron tunneling times in proteins [cyt *c* (○); azurin (▽); cyt b_{562} (□); myoglobin (△); and high-potential iron–sulfur protein (◇)] fall in the 1.0- to 1.2-Å^{-1} wedge (pale blue solid lines; pale blue dashed line is the average β of 1.1 Å^{-1}). Colored circles (*Zn-cyt *c* → Fe(III)-cyt *c*, green and Fe(II)-cyt *c* → Zn-cyt *c*$^+$, red) are interprotein time constants.

CcP–cyt *c* complexes. Electron tunneling across hydrogen-bonded interfaces is well established (33–35), and the coupling across one or two water molecules (<5 Å) should not be much weaker than that over a comparable distance of peptide (36). Our finding that the ET rates for **R2** and **R3** fall well within the range that has been established for Ru proteins with similar donor–acceptor separations (Fig. 5; ref. 36) indicates that small interaction zones, such as that between Zn-cyt *c* and Fe-cyt *c*, are quite effective in mediating interprotein redox reactions.

Integrating photosensitizers into protein crystals provides a powerful tool for studying biochemical reaction dynamics. Indeed, the applications of this methodology could extend well beyond the bounds of interprotein ET kinetics. Zn-cyt *c* should be an excellent optical trigger for time-resolved x-ray crystallography, a technique that requires rapid and efficient initiation of a reaction throughout the x-ray beam cross section in the sample (37, 38). The long-lived, strongly reducing triplet excited state ($\phi_{*\text{Zn-cyt } c} = 0.9$) of Zn-cyt *c* leads to high quantum yields for ET ($\phi_{ET} \approx 0.7$ in our system). Introduction of Zn-porphyrins thus creates opportunities to probe redox-induced structural changes and catalytic intermediates in protein crystals.

We thank D. C. Rees and the Stanford Synchrotron Research Laboratory for access to data collection facilities, and A. M. Bilwes for technical assistance and helpful discussions. B.R.C. acknowledges the Helen Hay Whitney Foundation for a postdoctoral fellowship. This work was supported by the National Science Foundation and the Arnold and Mabel Beckman Foundation.

1. Langen, R., Chang, I.-J., Germanas, J. P., Richards, J. H., Winkler, J. R. & Gray, H. B. (1995) *Science* **268,** 1733–1735.
2. Gray, H. B. & Winkler, J. R. (1996) *Annu. Rev. Biochem.* **65,** 537–561.
3. Winkler, J. R., DiBilio, A. J., Farrow, N. A., Richards, J. H. & Gray, H. B. (1999) *Pure Appl. Chem.* **71,** 1753–1764.
4. Winkler, J. R. (2000) *Curr. Opin. Chem. Biol.* **4,** 192–198.
5. Mei, H., Wang, K., Peffer, N., Weatherly, G., Cohen, D. S., Miller, M., Pielak, G. J., Durham, B. & Millett, F. (1999) *Biochemistry* **38,** 6846–6854.
6. Farver, O. & Pecht, I. (1997) *J. Biol. Inorg. Chem.* **2,** 387–392.
7. Dick, L. A., Malfant, I., Kuila, D., Nebolsky, S., Nocek, J. M., Hoffman, B. M. & Ratner, M. A. (1998) *J. Am. Chem. Soc.* **120,** 11401–11407.
8. Beratan, D. N., Betts, J. N. & Onuchic, J. N. (1991) *Science* **252,** 1285–1288.
9. Onuchic, J. N., Beratan, D. N., Winkler, J. R. & Gray, H. B. (1992) *Annu. Rev. Biophys. Biomol. Struct.* **21,** 349–377.
10. Beratan, D. N. & Skourtis, S. S. (1998) *Curr. Opin. Chem. Biol.* **2,** 235–243.
11. Daizadeh, I., Gehlen, J. N. & Stuchebrukhov, A. A. (1997) *J. Chem. Phys.* **106,** 5658–5666.
12. Moser, C. C., Keske, J. M., Warncke, K., Farid, R. S. & Dutton, P. L. (1992) *Nature (London)* **355,** 796–802.
13. Williams, R. J. P. (1997) *J. Biol. Inorg. Chem.* **2,** 373–377.
14. McLendon, G. & Hake, R. (1992) *Chem. Rev.* **92,** 481–490.
15. Nocek, J. M., Zhou, J. S., De Forest, S., Priyadarshy, S., Beratan, D. N., Onuchic, J. N. & Hoffman, B. M. (1996) *Chem. Rev.* **96,** 2459–2489.
16. Davidson, V. L. (2000) *Acc. Chem. Res.* **33,** 87–93.
17. Pletneva, E. V., Fulton, D. B., Kohzuma, T. & Kostic, N. M. (2000) *J. Am. Chem. Soc.* **122,** 1034–1046.
18. Adir, N., Axelrod, H. L., Beroza, P., Isaacson, R. A., Rongey, S. H., Okamura, M. Y. & Feher, G. (1996) *Biochemistry* **35,** 2535–2547.
19. Pelletier, H. & Kraut, J. (1992) *Science* **258,** 1748–1755.
20. Chen, L., Durley, R., Poliks, B. J., Hamada, K., Chen, Z., Mathews, F. S., Davidson, V. L., Satow, Y., Huizinga, E., Vellieux, F. M., *et al.* (1992) *Biochemistry* **31,** 4959–4964.
21. Chen, L., Durley, R. C., Mathews, F. S. & Davidson, V. L. (1994) *Science* **264,** 86–90.
22. Sevrioukova, I. F., Hazzard, J. T., Tollin, G. & Poulos, T. L. (1999) *J. Biol. Chem.* **274,** 36097–36106.
23. Takano, T. & Dickerson, R. E. (1980) *Proc. Natl. Acad. Sci. USA* **77,** 6371–6375.
24. Elias, H., Chou, M. H. & Winkler, J. R. (1988) *J. Am. Chem. Soc.* **110,** 429–434.
25. Sun, J., Su, C. & Wishart, J. F. (1996) *Inorg. Chem.* **35,** 5893–5901.

26. Otwinowski, Z. & Minor, W. (1997) *Methods Enzymol.* **276,** 307–326.
27. Brünger, A. T., Adams, P. D., Clore, G. M., DeLano, W. L., Gros, P., Grosse-Kunstleve, R. W., Jiang, J. S., Kuszewski, J., Nilges, M., Pannu, N. S., *et al.* (1998) *Acta Crystallogr. D* **54,** 905–921.
28. McRee, D. (1992) *J. Mol. Graphics* **10,** 44–46.
29. Connolly, M. L. (1983) *Science* **221,** 709–713.
30. Crane, B. R. & Getzoff, E. D. (1997) *Acta Crystallogr. D* **53,** 23–40.
31. Zemel, H. & Hoffman, B. M. (1981) *J. Am. Chem. Soc.* **103,** 1192–1201.
32. Lo Conte, L., Chothia, C. & Janin, J. (1999) *J. Mol. Biol.* **285,** 2177–2198.
33. de Rege, P. J. F., Williams, S. A. & Therien, M. J. (1995) *Science* **269,** 1409–1413.
34. Kirby, J. P., Roberts, J. A. & Nocera, D. G. (1997) *J. Am. Chem. Soc.* **119,** 9230–9236.
35. Yang, J., Seneviratne, D., Arbatin, G., Andersson, A. M. & Curtis, J. C. (1997) *J. Am. Chem. Soc.* **119,** 5329–5336.
36. Ponce, A., Gray, H. B. & Winkler, J. R. (2000) *J. Am. Chem. Soc.* **122,** 8187–8191.
37. Ren, Z., Bourgeois, D., Helliwell, J. R., Moffat, K., Srajer, V. & Stoddard, B. L. (1999) *J. Synchrotron Radiol.* **6,** 891–917.
38. Schlichting, I. (2000) *Acc. Chem. Res.* **33,** 532–538.